Sen Lin[1]
Department of Civil Engineering,
Johns Hopkins University,
Baltimore, MD 21218
e-mail: slin@jhu.edu

Longyu Zhao
Department of Materials Science
and Engineering,
Johns Hopkins University,
Baltimore, MD 21218

James K. Guest
Associate Professor
Department of Civil Engineering,
Johns Hopkins University,
Baltimore, MD 21218

Timothy P. Weihs
Professor
Department of Materials Science
and Engineering,
Johns Hopkins University,
Baltimore, MD 21218

Zhenyu Liu
Professor
Changchun Institute of Optics,
Fine Mechanics and Physics,
Chinese Academy of Sciences,
Changchun, Jilin 130033, China

Topology Optimization of Fixed-Geometry Fluid Diodes

This paper proposes using topology optimization to design fixed-geometry fluid diodes that allow easy passage of fluid flowing in one direction while inhibiting flow in the reverse direction. Fixed-geometry diodes do not use movable mechanical parts or deformations, but rather utilize inertial forces of the fluid to achieve this flow behavior. Diode performance is measured by diodicity, defined as the ratio of pressure drop of reverse flow and forward flow, or equivalently the ratio of dissipation of reverse and forward flow. Diodicity can then be maximized by minimizing forward dissipation while maximizing reverse dissipation. While significant research has been conducted in topology optimization of fluids for minimizing dissipation, maximizing dissipation introduces challenges in the form of small, mesh dependent flow channels and that artificial flow in solid region becomes (numerically) desirable. These challenges are circumvented herein using projection methods for controlling the minimum length scale of channels and by introducing an additional penalty term on flow through intermediate porosities. Several solutions are presented, one of which is fabricated by 3D printing and experimentally tested to demonstrate the diodelike behavior. [DOI: 10.1115/1.4030297]

Keywords: fluid diode, Tesla valve, topology optimization, dissipation, projection methods, Navier–Stokes equations

1 Introduction

Check valves are devices that control flow direction in fluid systems. They can generally be grouped into three categories according to their actuation mechanism: active valves feature moving parts that are actuated by external forces; passive valves (such as Domino valves in Ref. [1]) are actuated by fluid motion; fixed-geometry or no-moving-part (NMP) valves rely not on moving parts or deformation, but rather utilize fluidic inertial forces to inhibit flow in the undesirable direction. Passive and fixed-geometry valves are often referred to as fluid diodes.

This paper studies fixed-geometry fluid diodes with flat-walled structures (denoted as fluid diode for brevity hereafter), of which the Tesla valve and diffuser are examples. A Tesla valve (Fig. 1(*a*)) is composed of a straight and a bowed channel arranged such that flow in the forward direction is "easy" and flow in the reverse direction is inhibited [2]. The idea is that the fluid enters the straight channel in the forward flow case and takes a relatively straight path toward the outlet port (Fig. 2(*a*)). In the reverse flow case, inertial forces drive fluid into the bowed channel as shown in Fig. 2(*b*), which is a longer and curved path to the outlet thereby dissipating significant energy. This makes the required driving pressure for flow in the reverse direction significantly larger than that in the forward direction, creating a diode effect. A diffuser (Fig. 1(*a*)) is a flow channel with expanding cross section, which exhibits similar behavior as flow in the direction of the expansion requires significantly less driving pressure than flow in the reverse direction. The difference between Tesla valves and diffusers is the outlet/inlet width. In this work we not only recreate the Tesla valve, but also create new, quite different topologies, which we refer to broadly as fluid diodes.

Although fixed-geometry diodes significantly inhibit fluid flow in the reverse direction, they do not eliminate reverse flow. However, they offer other advantages over active valves, including improved manufacturability, robustness, and external power independence, and they are capable of handling particle-laden, multiphase, and oscillating flows. They are, therefore, employed in a number of applications: [3] integrated Tesla valve into a flat-plate oscillating heat pipe to achieve circulatory flow; [4,5] constructed miniature valveless membrane pumps using Tesla valve as fluidic rectifiers; diffusers are frequently used in fluid pumps as in Refs. [6–8].

Significant research on Tesla valves and diffusers has been conducted. Reference [9] analyzed the diodicity (ratio of pressure drop of reverse flow to that of forward flow) mechanism of Tesla valve at low Reynolds number and proposed several guidelines on

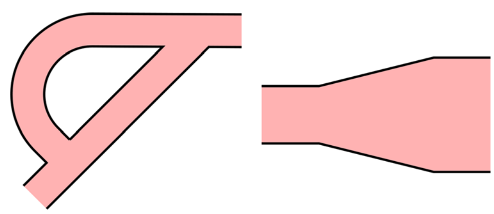

(a) Tesla valve (b) Diffuser

Fig. 1 Fixed-geometry fluid diodes with flat-walled structures: (*a*) Tesla valve and (*b*) diffuser

[1]Corresponding author.

Contributed by the Design Automation Committee of ASME for publication in the JOURNAL OF MECHANICAL DESIGN. Manuscript received November 10, 2014; final manuscript received March 25, 2015; published online June 8, 2015. Assoc. Editor: Kazuhiro Saitou.

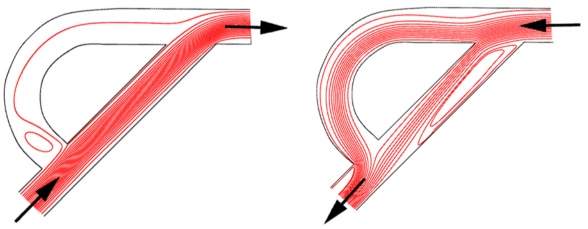

(a) Forward flow (b) Reverse flow

Fig. 2 Streamline of original Tesla valve (Re = 300): (*a*) forward flow and (*b*) reverse flow

improving Tesla valve; [10] using shape optimization achieved 25% higher diodicity at Reynolds number $1 < \mathrm{Re} \leq 2000$; literature on shape optimization of diffuser-type diodes can be found in (for example) Refs. [11–13].

This paper seeks to design fluid diodes using topology optimization with finite element method (FEM). Topology optimization is a systematic approach to optimizing the distribution of material (or fluid) across a design domain for a given set of boundary conditions and design constraints. Although originally developed for structural components, topology optimization was extended to fluid fields in Ref. [14] to minimize dissipation of fluids whose flow was governed by Stokes equations. Alternate formations were later proposed in Refs. [15–17] for slow incompressible flows, Ref. [18] for slightly compressible flows, and Refs. [19–23] for low-to-moderate Reynolds numbers. Of particular note is the work of Refs. [24] and [25], which combined Lattice–Boltzmann (LBM) method with topology optimization framework to design Tesla-valves featuring conceptually novel design layouts. A key difference in the proposed work is the use of FEMs and we focus on aligned inlet and outlet ports of identical size, which facilitates connecting the diodes in series to enhance system diodicity.

2 Topology Optimization

2.1 Governing Equation. The topology optimization process begins by discretizing the design domain using finite elements, herein chosen as quadrilateral elements. Numerical stability is achieved using Q_2-Q_1 elements (Taylor–Hood method), where velocity and pressure are approximated with biquadratic and bilinear shape functions, respectively (see Ref. [26] for additional details).

The goal is to then determine the local porosity of each finite element, denoted as γ_i, with $\gamma_i = 1$ indicating the element is a pore and thus a fluid channel, and $\gamma_i = 0$ indicating that the element contains solid material. The design problem is therefore a binary programing problem, further complicated by the no-slip condition being a discrete moving-boundary condition [14,15].

In order to use gradient-based optimization algorithms, the design variables γ_i are permitted to take value continuously from 0 to 1 and the discrete no-slip condition is approximated as a continuous function. This is achieved by treating the solid phase as a permeable material, thereby allowing flow through the solid phase and intermediate phases. Reference [14] achieved this using a Darcy damping force $\mathbf{f} = -\alpha \mathbf{u}$, where α is the degree of local impermeability, which was then added to the governing Stokes

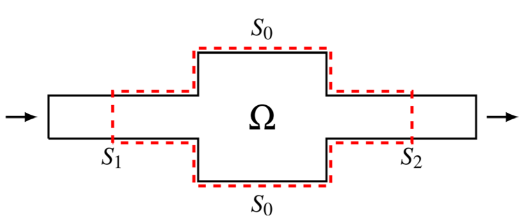

Fig. 3 Demonstration of the control volume Ω, shown as dashed line

equations. In the context of Navier–Stokes equations, this yields the following governing equations:

$$\rho(\mathbf{u} \cdot \nabla)\mathbf{u} = -\nabla p + \mu \nabla^2 \mathbf{u} - \alpha(\gamma)\mathbf{u} \tag{1}$$

In Eq. (1), the physical meaning of α can be interpreted as local impermeability and it is related with material porosity γ via [14]

$$\alpha(\gamma) = \underline{\alpha} + (\bar{\alpha} - \underline{\alpha}) \frac{q(1-\gamma)}{q+\gamma} \tag{2}$$

where $\underline{\alpha}$ is the minimum allowable value of α, $\bar{\alpha}$ is the maximum allowable value, and q is a parameter to control convexity of $\alpha(\gamma)$. If $\bar{\alpha}$ is infinitely large, then Eq. (2) represents a nonpenetrable solid material. In this work, $\underline{\alpha} = 0$, $q = 10^5$, and $\bar{\alpha}$ is set to be a large number, as described in the following sections.

As for the boundary conditions of the domain, let us examine Fig. 3 which gives a demonstration of the forward case: inlet is the leftmost vertical boundary with an arrow pointing in; outlet is the rightmost vertical boundary with an arrow pointing out; all the other boundaries are set to be wall with no-slip boundary condition ($\mathbf{u} = 0$ at the wall). In the reverse case, we switch inlet and outlet while keeping the other boundaries unchanged. In both directions, the inlet boundary condition is set to be fixed velocity with parabolic flow profile, and the outlet is prescribed as the reference pressure ($p = 0$).

2.2 Diodicity Formulation. Performance of fluid diode is measured by diodicity, which is defined as the ratio of pressure drop of reverse flow to that of the forward flow while fixing the flow rate

$$\mathrm{Di} = \Delta p_r / \Delta p_f \tag{3}$$

An alternative way to define diodicity is to fix driving pressure and take the ratio of flow rate of two directions. Although theoretically equivalent, the best way to pose this problem is ultimately dependent on the target application. In this work, Eq. (3) is used primarily to match our existing experimental setup as described in Sec. 4.

Larger diodicity indicates better performance, and therefore we aim to maximize diodicity under the assumption of the Navier–Stokes equations. Although the ratio in Eq. (3) could be used directly as the objective function, it is generally more favorable in numerical optimization to choose an objective that takes the form of a volume integral of an energy function. Reference [14] proposed minimizing dissipation as the objective function under a constraint on the fluid volume fraction. Dissipation is given by

$$\Phi(\mathbf{u}, p) = \int_\Omega \left[\frac{\mu}{2} \sum_{i,j} \left(\frac{\partial u_i}{\partial x_j} + \frac{\partial u_j}{\partial x_i} \right)^2 \right] + \sum_i \alpha(\gamma) u_i^2 \tag{4}$$

where the first term of the integrand is viscous dissipation for incompressible Newtonian flow, and the second term is dissipation due to an artificial Darcy force.

Dissipation is closely related to pressure drop [14], and therefore diodicity as the ratio of pressure drop can be defined using dissipation. As shown in Fig. 3, the control volume Ω is selected in such a way that flows at the upstream cross section S_1 and downstream cross section S_2 are fully developed. The steady momentum equation is given as

$$\rho \mathbf{u} \cdot \nabla \mathbf{u} = -\nabla p + \nabla \cdot \tau - \alpha \mathbf{u} \tag{5}$$

Taking the dot product of Eq. (5) with $\mathbf{u}$ and using some other manipulations

$$\mathbf{u}\cdot\nabla p = \nabla\cdot(p\mathbf{u})$$
$$\mathbf{u}\cdot(\rho\mathbf{u}\cdot\nabla\mathbf{u}) = \nabla\cdot(\mathbf{u}\frac{1}{2}\rho\mathbf{u}^2)$$
$$\mathbf{u}\cdot(\nabla\cdot\tau) = \nabla\cdot(\tau\cdot\mathbf{u}) - \tau\colon\nabla\mathbf{u}$$

we can get the mechanical energy equation

$$\nabla\cdot\left(\mathbf{u}\frac{1}{2}\rho\mathbf{u}^2\right) = -\nabla\cdot(p\mathbf{u}) + \nabla\cdot(\tau\cdot\mathbf{u}) - \tau\colon\nabla\mathbf{u} - \alpha\mathbf{u}^2 \quad (6)$$

where $\tau\colon\nabla\,\mathbf{u}$ is viscous dissipation. For incompressible Newtonian fluid $\tau = \mu[\nabla\mathbf{u} + (\nabla\mathbf{u})^{\mathrm{T}}]$, and

$$\tau\colon\nabla\mathbf{u} = \mu(\partial_i u_j + \partial_j u_i)\partial_j u_i = \sum_{i,j}\frac{\mu}{2}(\partial_j u_i + \partial_i u_j)^2 \quad (7)$$

which is exactly the same as the first term of integrand in Eq. (4). Therefore, the energy equation can be rewritten as

$$\tau\colon\nabla\mathbf{u} + \alpha\mathbf{u}^2 = \nabla\cdot(\tau\cdot\mathbf{u} - p\mathbf{u} - \frac{1}{2}\rho\mathbf{u}^2\mathbf{u}) \quad (8)$$

Integrating Eq. (8) over the control volume Ω and employing the Divergence Theorem gives

$$\Phi = \int_\Omega \tau\colon\nabla\mathbf{u} + \alpha\mathbf{u}^2 = \int_{\partial\Omega}\left[\mathbf{n}\cdot\tau\cdot\mathbf{u} - p(\mathbf{u}\cdot\mathbf{n}) - \frac{1}{2}\rho\mathbf{u}^2(\mathbf{u}\cdot\mathbf{n})\right] \quad (9)$$

where the boundary $\partial\Omega$ is composed of three segments, $\partial\Omega = S_0 \cup S_1 \cup S_2$. Due to the no-slip boundary condition on S_0, we have

$$\Phi = \int_{S_1+S_2}\left[\mathbf{n}\cdot\tau\cdot\mathbf{u} + p(-\mathbf{u}\cdot\mathbf{n}) + \frac{1}{2}\rho\mathbf{u}^2(-\mathbf{u}\cdot\mathbf{n})\right] \quad (10)$$

The three terms can be greatly simplified for fully developed flow. The first term means work done by viscous stress. Since $\mathbf{u}$ and $\mathbf{n}$ are either in the same or opposite direction, it vanishes in fully developed flow

$$\mathbf{u}\cdot(\tau\cdot\mathbf{n}) = \pm u(\mathbf{n}\cdot\tau\cdot\mathbf{n}) = \pm u\tau_{nn} = 0 \quad (11)$$

As pressure is constant along cross-stream direction of fully developed flow, the second term, which is work done by pressure drop, can be rewritten as

$$\int_{S_1+S_2} p(-\mathbf{u}\cdot\mathbf{n})\mathrm{d}S = p_1\int_{S_1} u\mathrm{d}S - p_2\int_{S_2} u\mathrm{d}S = \Delta p\cdot Q \quad (12)$$

where $Q = \int_{S_1} u\mathrm{d}S = \int_{S_2} u\mathrm{d}S$ is the flow rate and $\Delta p = p_1 - p_2$ is the pressure drop between S_1 and S_2. The third term is interpreted as mechanical energy convected into the control volume, and its integral is zero due to the same velocity profiles at S_1 and S_2. Therefore, we get the final simplified form

$$\Phi(\mathbf{u}, p) = \Delta p\cdot Q \quad (13)$$

Equation (13) simply means that the power dissipated in the control volume Ω is equal to the work done by the driving pressure. Then diodicity can be redefined as the ratio of dissipations

$$\mathrm{Di}' = \frac{\Phi(\mathbf{u}_r, p_r)}{\Phi(\mathbf{u}_f, p_f)} = \frac{\Delta p_r\cdot Q_r}{\Delta p_f\cdot Q_f} = \frac{\Delta p_r}{\Delta p_f} = \mathrm{Di} \quad (14)$$

From $\Delta p \sim \rho U^2$ for fast flow or $\Delta p \sim \mu U/L$ for viscous dominated flow, we can conclude that if flow rate of forward and reverse flows are the same, the ratio of dissipations must be bounded, and Di' in Eq. (14) can thus serve as objective function. It is worth mentioning that in practice it is difficult to ensure that flows at the upstream and downstream cross sections are fully developed, but this is also not necessary. In this case $\mathrm{Di}' \approx \mathrm{Di}$.

2.3 Artificial Flow Penalty. The material interpolation scheme of Eqs. (1) and (2) allows fluid to penetrate elements having $\gamma_i < 1$, where $\gamma_i = 0$ indicates the element is wholly solid and $0 < \gamma_i < 1$ indicates the element contains a (fictitious) mixture of solid and void phases. Such behavior is often referred to as artificial flow [27]. In past work where the design objective is to minimize dissipation, solutions naturally tend toward 0-1 (solid-void) distributions of material when using this interpolation scheme with a relatively large magnitude of $\bar{\alpha}$. In the case of maximizing diodicity, however, initial results revealed that the algorithm designed small pockets of intermediate porosities in regions primarily accessed by the reverse flow case, thereby maximizing dissipation for the reverse flow case without significantly impacting dissipation in the forward flow case.

To eliminate these small pockets of intermediate porosities, a penalty term is added to the objective function to penalize the flow through the solid and intermediate phases in the reverse direction. This penalization is not needed in the forward flow case as minimizing forward dissipation naturally discourages artificial flow in the considered problems (although it is noted this may not always be the case [27]). Let us define a nondimensional Darcy term F_* as

$$F_* = \frac{1}{L^2}\int_\Omega \frac{\alpha\cdot||\mathbf{u}_r||_2}{\bar{\alpha}U} \quad (15)$$

where U is characteristic velocity (average velocity at the inlet) and W_F is a weighting coefficient. The objective function is then posed as minimizing $(1/\mathrm{Di}' + W_F\cdot F_*)$. As F_* is scaled to the similar order of magnitude as $\mathrm{Di}' \sim 1$, the coefficient should be chosen as $W_F \sim 1$ ($W_F = 3$ is used in this work).

2.4 Minimum Length Scale Control. Unlike topology optimization for minimum dissipation [14,15], the maximum diodicity design problem tends to prefer multiple small channels that are utilized in the reverse flow case. This leads to an issue of solution mesh dependence, where smaller channels develop as the finite element mesh is refined, similar to maximum stiffness problems in solid mechanics [28]. Projection methods, originally proposed in Ref. [29], have a demonstrated capability of circumventing this issue by imposing a minimum length scale on designed features. Herein we impose the length scale on the void phase to constrain channel sizes to a minimum radius of $R_{\min}$, and the projection method then mimics the fabrication process of etching [30,31]. This is achieved by introducing a set of variables ϕ that serve as the independent design variables for the optimization problem. These variables, located at the element centroids herein, are then mapped radially onto the finite element space to determine topology, making element porosities a function of these independent variables $\gamma(\phi)$. We utilize the formulation in Ref. [31] which, adjusting for the fact that the traditional topology optimization variable ρ means relative density and thus $\rho = 1 - \gamma$, is given as

$$\gamma = 1 - \exp(-\beta\cdot w(\phi)) + w(\phi)\cdot\exp(-\beta) \quad (16)$$

where $w(\phi)$ are the filtered (averaged) design variables within a distance $R_{\min}$ of the element centroid, weighted according to standard linear distance weighting functions [32], and β is the regularization parameter chosen here as $\beta = 10$ and kept constant following [33]. We note that a similar effect can be achieved using the erode filter of Ref. [30], which subtracts $w(\phi)$ from unity before passing it through the Heaviside function. Complete details of the employed projection methodology are provided in Ref. [31].

2.5 Optimization Formulation. In summary, the topology optimization design problem is stated formally as follows:

$$\min: 1/\mathrm{Di}' + W_F \cdot F_* \tag{17a}$$

$$\text{s.t.}: \rho(\mathbf{u}_f \cdot \nabla)\mathbf{u}_f = -\nabla p_f + \mu\nabla^2\mathbf{u}_f - \alpha(\gamma(\phi))\mathbf{u}_f \tag{17b}$$

$$\nabla \cdot \mathbf{u}_f = 0 \tag{17c}$$

$$\rho(\mathbf{u}_r \cdot \nabla)\mathbf{u}_r = -\nabla p_r + \mu\nabla^2\mathbf{u}_r - \alpha(\gamma(\phi))\mathbf{u}_r \tag{17d}$$

$$\nabla \cdot \mathbf{u}_r = 0 \tag{17e}$$

$$0 \le \phi \le 1 \tag{17f}$$

$$\int_\Omega \gamma(\phi) \le V_{\max} \cdot \int_\Omega 1 \tag{17g}$$

where $V_{\max}$ is the maximum allowable porosity in the design domain. This problem is solved using the method of moving asymptotes (MMA) introduced in Ref. [34].

It is worth noting that that the choice of $V_{\max}$ has a large influence on solutions when solving the traditional minimum dissipated power problem, and larger magnitudes of this variable lead to smaller magnitudes of dissipated power. When maximizing diodicity, however, solutions must contain some solid material in order to create a diode effect, and thus solutions are less dependent on the choice of $V_{\max}$, provided it is sufficiently large. While ideally one could simply relax this constraint, the optimizer tends to remove all material within the first few iterations when doing this, as open channel flow is a local minimum. We therefore chose $V_{\max} = 0.8$ for all examples, and note that this constraint is not always active in the considered examples. Of course one may also prefer to use a smaller $V_{\max}$ if lower fluid volume fractions are desired.

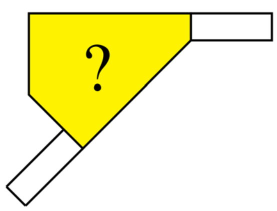

(a) Pentagon design domain with inclined inlet and outlet.

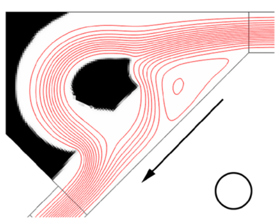

(b) Optimization result using projection method on fluid phase.

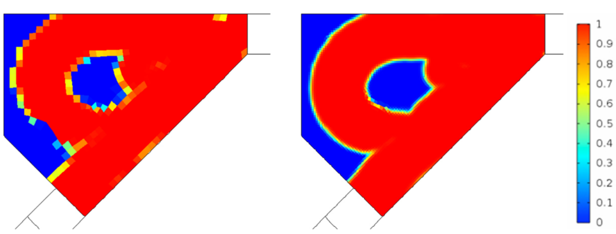

(c) Demonstration of mesh independency of projection method. Projection radius: $L/5$; mesh size: $L/6$ (left) and $L/20$ (right)

Fig. 4 Reproduction of the Tesla valve created using topology optimization (Re = 100; Da = 4.4 × 10^{-7}; W_F = 0; $R_{\min}$ = 0.25 L). The white circle shows projection diameter and the red lines represents streamlines of reverse flow. (*a*) Pentagon design domain with inclined inlet and outlet. (*b*) Optimization result using projection method on fluid phase. (*c*) Demonstration of mesh independency of projection method. Projection radius: *L*/5; mesh size: *L*/6 (left) and *L*/20 (right).

2.6 Optimization Parameters. It is useful to discuss results in terms of the Reynolds number occurring at the inlet of the design domain. Reynolds number is defined as the ratio of inertial to viscous effects and is given as

$$\mathrm{Re} = \frac{\rho U^2}{\mu U/L} = \frac{\rho U L}{\mu} \tag{18}$$

Although diodicity typically increases with Reynolds number as inertial forces become very large, accurate solution of the Navier–Stokes equation becomes challenging and computationally prohibitive for very large Reynolds number. In this study, we focus on solving the problem for cases of $100 \le \mathrm{Re} \le 300$, which we have found sufficient to generate significant diodicity effects without encountering challenges in solving the Navier–Stokes equations. It is worth mentioning that local Reynolds number within optimized topologies may be larger than the inlet Reynolds number, as channel width at some positions may be quite small. This serves as additional motivation for restricting the overall Reynolds number to be below 300. All asymptote parameters in MMA are chosen as discussed in Ref. [33].

It is well known that the magnitude of the permeability variable $\bar{\alpha}$ may influence the final solution. If chosen too small (artificial), flow is too large through the solid phase, and if chosen too large, the algorithm may converge to a low quality local minimum. Let us define the Darcy number as the ratio of viscous force to Darcy damping force as follows:

$$\mathrm{Da} = \frac{\mu U/L}{\bar{\alpha} L U} = \frac{\mu}{\bar{\alpha} L^2} \tag{19}$$

The variable $\bar{\alpha}$ can then be computed from Da. Following standard continuation strategies in Refs. [14,15], Da is decreased gradually as the optimization progresses from a relatively large value to a sufficiently small one ($\mathrm{Da} \sim 10^{-5}$).

3 Examples and Discussion

3.1 Reproducing the Tesla Valve. The first example we consider is the pentagon design domain with inclined inlet and horizontal outlet shown in Fig. 4(*a*), meant to answer the interesting question of whether we can reproduce the Tesla valve using the proposed approach. As previously mentioned, in this and all following examples, inlet flow conditions are prescribed to be fully developed flow with parabolic velocity profile and the outlet pressure is set to a reference pressure of $p = 0$.

The optimal solution found using topology optimization is shown in Fig. 4(*b*) using a relatively large minimum channel length scale as shown in the figure. The result clearly resembles the original valve design by Nicola Tesla (Fig. 1(*a*), also Ref. [2]). Figures 4(*c*) and 4(*d*) display solutions using two different finite element discretizations: a coarse mesh with element size $L/6$ and a refined mesh with element size $L/20$ (an order of magnitude more elements). The refined mesh has smoother boundaries but the same overall topology when using the same prescribed (relatively large) minimum length scale of the channel. In the case where this length scale is relaxed, and smaller features are permitted to form, more intricate solutions will lead to improved diodicity at the cost of larger pressure drop. One could perhaps constrain pressure

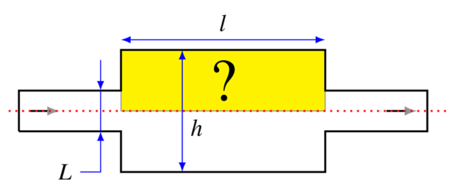

Fig. 5 Demonstration of the rectangular design domain

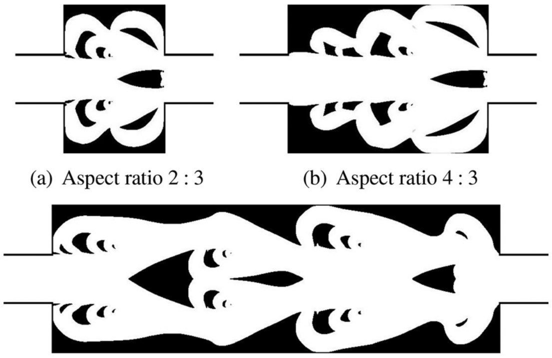

(a) Aspect ratio 2 : 3 (b) Aspect ratio 4 : 3

(c) Aspect ratio 9 : 3

Fig. 6 Optimization results for different aspect ratio (Re = 300, Da = 3×10^{-5}, W = 0.1). (*a*) Aspect ratio 2:3; (*b*) aspect ratio 4:3; and (*c*) aspect ratio 9:3.

drop without length scale control to recover the Tesla valve design, although this is not performed here.

3.2 Design of Diodes With Aligned Inlet and Outlet. The next design examples consider the case of inlet and outlet channels being aligned, as shown in Fig. 5, with symmetry employed as indicated by the highlighting. We also relax the minimum length scale constraint by setting $\gamma = \phi$. Various aspect ratios of l:h are considered. The requirement of aligned flow channels makes designing a diode more challenging, but also facilitates placement of diodes within a straight flow system or serially combining them in a compact manner to enhance diodicity. Of course the original Tesla valves could also be used in series as shown in Refs. [24] and [25], which would lead to a simpler topology with larger pressure drops but also smaller diodicities.

Figure 6 gives topology-optimized solutions for several different aspect ratios. Although the diode designs change with aspect ratio, they all utilize common features in the designs. These include systems of looped pipes, as used in the original Tesla valve, and objects placed in the center of the main flow channel that feature a smooth forward end and a wall-like feature on the back end, reducing drag in the forward flow case and inhibiting flow in the reverse flow case. We note that in some applications, such as Ref. [3], it is favorable to adopt long fluid diodes that can also serve as flow channel. The solution in Fig. 6(*c*), found using a domain aspect ratio of 9:3, may be useful in such applications.

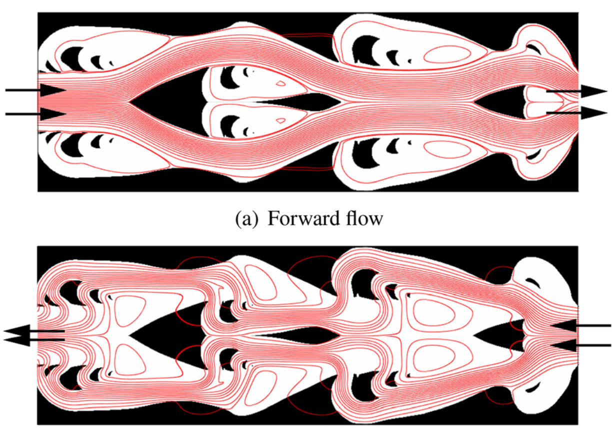

(a) Forward flow

(b) Reverse flow

Fig. 7 Streamlines of the optimized fluid diode shown in Fig. 6(*c*) (Re = 300, Da = 3×10^{-5}, aspect ratio = 9:3). (*a*) Forward flow and (*b*) reverse flow.

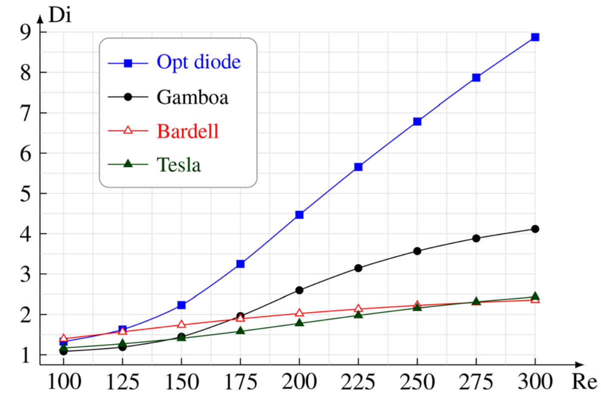

Fig. 8 Comparison of diodicity of channel-like diode and published works (simulation result)

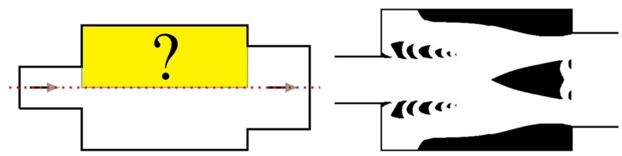

(a) Design domain (b) Optimization result

Fig. 9 Optimization result with expanding channel (Re = 300, Da = 3×10^{-5}, W = 0.1, aspect ratio 4:3). (*a*) Design domain and (*b*) optimization result.

The streamlines for the forward and reverse flow of the solution in Fig. 6(*c*) are shown in Fig. 7. It is clearly seen that the fluid takes a subtly winding path in the forward direction. This is in contrast to the reverse case where the fluid is continuously steered by inertial forces into the smaller, curved side flow channels. The diodicity of this solution is compared against the original Tesla valve [2] and later modifications proposed in Refs. [9] and [10] for different Reynolds numbers in Fig. 8. The topology-optimized design clearly exhibits larger diodicity, particularly as fluid inertial forces increase with larger Reynolds number.

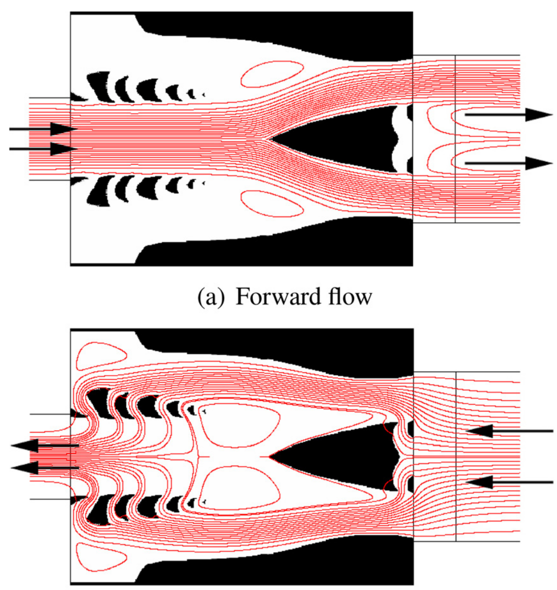

(a) Forward flow

(b) Reverse flow

Fig. 10 Streamlines of optimized diffuser-type diode (Re = 300, Da = 3×10^{-5}). (*a*) Forward flow and (*b*) reverse flow.

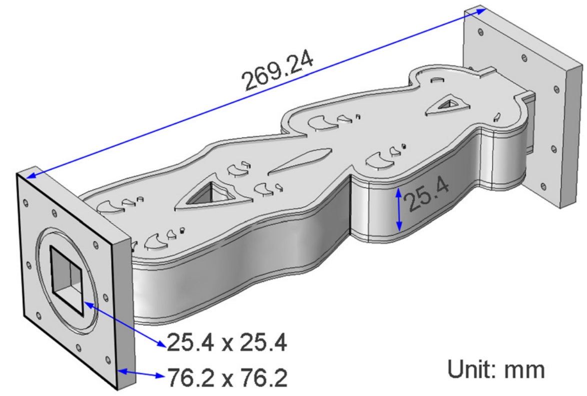

(a) Geometry for 3D printing

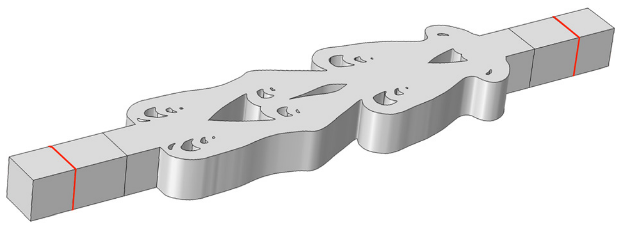

(b) 3D representation of the void (fluid) space for the experiment, with locations of pressure measurement marked as red.

Fig. 11 Fabricated fluid diode specimen. (*a*) Geometry for 3D printing (*b*) 3D representation of the void (fluid) space for the experiment, with locations of pressure measurement marked as red.

3.3 Fluid Diode With Expanding Channel. As a final example, we consider a fluid diode with expanding channel, which could be classified as a diffuser-type diode. The outlet on the right boundary is increased to double the size of the left channel as shown in Fig. 9(*a*). The topology-optimized solution is shown in Fig. 9(*b*) and corresponding streamlines in Fig. 10. We again see that the fluid takes a smooth, slightly curved path in the forward flow case and gets diverted into the smaller side channels, requiring a sharp turn to reach the outlet, in the reverse flow case. This combination leads to a large diodicity of 20.

4 Experimental Testing

In order to confirm that the designed device performs as a diode, the optimized design in Fig. 6(*c*) was extruded a distance z to a 3D model and fabricated by 3D printing. Figure 11(*a*) shows the specimen, whose interior void space constitutes flow channels as shown in Fig. 11(*b*). Both ends of the specimen are connected to square cross section conduits, and then flow rates and pressure drops are measured between the two positions marked as red in Fig. 11(*b*). The sample was tested three times. In the experiments, pressure drop was measured with an OMEGA HHP-803/SIL differential pressure meter to an accuracy of ± 0.01 psi and flow rate measurement was achieved with beaker and stopwatch. In order to reach the designated Reynolds number range and also to yield measurable pressure drops, a mixture of polyethylene glycol (PEG) 400 and de-ionized water was used as working fluid with viscosity 37.6 ± 0.1 cP and density 1.05 ± 0.03 g/mL at 19.8 °C measured by a Brookfield LVDV-II + PRO viscometer before and after the testing.

By measuring flow rate and pressure drop of both flow directions and using interpolation, we can calculate a curve of Diodicity versus Reynolds number as shown in Fig. 12. Although the specimen clearly exhibited diodelike behavior, the measured diodicity is smaller than that in Fig. 8. The primary reason for this discrepancy is that extruded height z of the specimen was

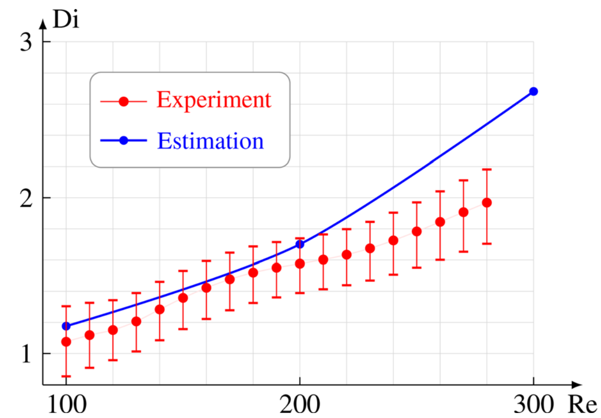

Fig. 12 Diodicity versus Reynolds number calculated via interpolation of experimental measurements (red curve) and computational simulations for the three-dimensional extruded sample with distanced pressure measurement locations (blue curve). The experimental error bars represent the combination of variation from three experimental trials and the accuracy of the instruments.

relatively small, thus violating the 2D simplification that assumed the top and bottom surface walls had negligible influence on the fluid flow. Additionally, the locations of pressure measurements were significantly farther upstream and downstream than assumed in the optimization. A three-dimensional finite element analysis was performed to evaluate the effect of these differences and the results are shown by the blue curve in Fig. 13. These simulations are in good agreement with the experimental results, suggesting they are the primary drivers for the reduction in diodicity. We emphasize, however, that the dimensions of the 3D printed sample (Fig. 11(*a*)), and particularly the relatively small extrusion height z to length l ratio, were selected here only to conform to an existing experimental setup. It is expected that increasing the z/l ratio would increase the measured diodicity. In the event that a specific application requires a small z/l ratio, the 2D assumption is no

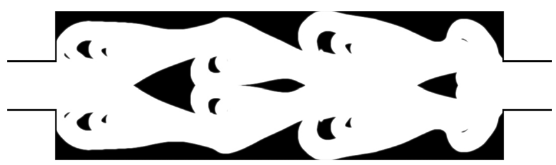

(a) Dilation. Di = 7.41

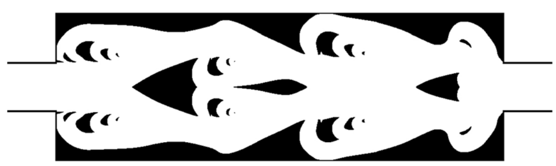

(b) Original. Di = 8.87

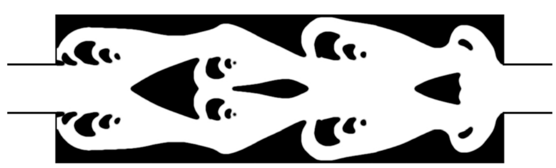

(c) Erosion. Di = 4.24

Fig. 13 Demonstration of the impact of fabrication errors at Re = 300. Small perturbations in channel sizes lead to loss in diodicity, with smaller channel sizes (over deposition of 3D printed material) leading to a 50% loss in diodicity. (*a*) Dilation, Di = 7.41; (*b*) Original, Di = 8.87; (*c*) Erosion, Di = 4.24.

longer valid and one would need to perform the topology optimization in three dimensions.

Additional sources of discrepancy between the predicted and experimental measurements may be due to surface roughness of the 3D printed specimen and manufacturing imperfections. To estimate the effect of general manufacturing variations, we perturbed the design of Fig. 6(*c*) using erode and dilate filters following the idea of Ref. [35] to simulate over and under etching, or in this case under and over deposition of material. These filters created the topologies shown in Fig. 13. Interestingly, varying the design from the optimized version, by either increasing or decreasing channel sizes slightly, led to performance losses. Thinning the channels, which corresponds to 3D printed features that are larger than desired, decreased the diodicity by over 50%. This emphasizes the importance of including the possibility of such variations in the problem formulation, referred to as robust topology optimization [35–39].

5 Concluding Remarks

The free-form nature of topology optimization was leveraged to design fixed-geometry fluid diodes. Diodicity was measured by the ratio of pressure drop when fluid flows in the reverse direction to pressure drop in the forward direction, or equivalently the ratio of dissipation of fluid flowing in the reverse direction to dissipation in the forward direction. The algorithm then essentially attempts to maximize dissipation in the reverse direction without significantly increasing dissipation when flowing in the forward direction.

The topology optimization algorithm was able to recreate the geometry invented by Nicola Tesla [2] when imposing a large minimum length scale on the channel size and orienting the inlet and outlet channels as Tesla did. However, new topologies with significantly improved diodicity were discovered when relaxing these restrictions, including cases where inlet and outlet channels are aligned to facilitate connecting these diodes in series, or to existing (straight) piping systems. Interestingly, the optimized solutions exhibited similar features of sharp, curved channels that only become a significant flow channel in the reverse flow case.

The optimized design of Fig. 6(*c*) was also fabricated with 3D printing and experimentally tested. Although diodicity was less than predicted by the 2D approximation, the experimental results confirmed the specimen behaved as a fluid diode. The discrepancy was primarily due to the limited extrusion height of the specimen which was required to conform to an existing experimental apparatus. While these results are promising, a number of challenges still remain, including optimizing for larger Reynolds numbers than considered here, where increased inertial forces should further amplify diodicity.

Acknowledgment

The authors thank Andrew Gaynor (JHU) for his assistance in fabricating the experimentally tested diode. This work was supported in part by the National Science Foundation under Grant No. CMMI-1400394 and the DARPA (Defense Advanced Research Projects Agency) under Project No. DAA-10-16. These supports are gratefully acknowledged.

Nomenclature

- Da = Darcy number
- Di = diodicity
- F_* = penalty term for artificial flow
- h = height of the rectangular design domain
- l = length of the rectangular design domain
- L = characteristic length (inlet width)
- q = material interpolation parameter
- $p_f, \mathbf{u}_f$ = pressure and velocity of forward flow
- $p_r, \mathbf{u}_r$ = pressure and velocity of reverse flow
- $R_{\min}$ = the minimum length scale (radius) of designed features
- Re = Reynolds number
- U = characteristic velocity (average velocity at the inlet)
- $V_{\max}$ = maximum allowable fluid volume fraction (between 0 to 1)
- $w(\phi)$ = filtered design variables corresponding to elements
- W_F = weighting factor of F_*
- z = extruded height of the 3D printed specimen
- α = material impermeability
- $\underline{\alpha}, \bar{\alpha}$ = minimum and maximum allowable value of α
- β = Heaviside Projection regularization parameter
- γ = elemental porosity
- μ = dynamic viscosity
- ϕ = independent design variables
- Φ = total dissipation
- ρ = density of fluid

References

[1] Sochol, R. D., Glick, C. C., Lee, K. Y., Brubaker, T., Lu, A., Wah, M., Gao, S., Hicks, E., Wolf, K. T., Iwai, K., Lee, L. P., and Lin, L., 2013, "Single-Layer "domino" Diodes Via Optofluidic Lithography for Ultra-Low Reynolds Number Applications," 2013 IEEE 26th International Conference on Micro Electro Mechanical Systems (MEMS), IEEE, pp. 153–156.

[2] Tesla, N., 1920, Valvular Conduit, Feb. 3, U.S. Patent No. 1,329,559.

[3] Thompson, S., Ma, H., and Wilson, C., 2011, "Investigation of a Flat-Plate Oscillating Heat Pipe With Tesla-Type Check Valves," Exp. Therm. Fluid Sci., **35**(7), pp. 1265–1273.

[4] Forster, F. K., Bardell, R. L., Afromowitz, M. A., Sharma, N. R., and Blanchard, A., 1995, "Design, Fabrication and Testing of Fixed-Valve Micro-Pumps," The ASME Fluid Engineering Division, Vol. 234, pp. 39–44.

[5] Morganti, E., and Pignatel, G., 2005, "Microfluidics for the Treatment of the Hydrocephalus," Proceedings of International Conference on Sensing Technology, Palmerston North.

[6] Stemme, E., and Stemme, G., 1993, "A Valveless Diffuser/Nozzle-Based Fluid Pump," Sens. Actuators, A, **39**(2), pp. 159–167.

[7] Andersson, H., van der Wijngaart, W., Nilsson, P., Enoksson, P., and Stemme, G., 2001, "A Valve-Less Diffuser Micropump for Microfluidic Analytical Systems," Sens. Actuators, B, **72**(3), pp. 259–265.

[8] Olsson, A., Enoksson, P., Stemme, G., and Stemme, E., 1997, "Micromachined Flat-Walled Valveless Diffuser Pumps," J. Microelectromech. Syst., **6**(2), pp. 161–166.

[9] Bardell, R. L., 2000, "The Diodicity Mechanism of Tesla-Type No-Moving-Parts Valves," Ph.D. thesis, University of Washington, Seattle.

[10] Gamboa, A. R., Morris, C. J., and Forster, F. K., 2005, "Improvements in Fixed-Valve Micropump Performance Through Shape Optimization of Valves," ASME J. Fluids Eng., **127**(2), pp. 339–347.

[11] Clabuk, H., and Modi, V., 1992, "Optimum Plane Diffusers in Laminar Flow," J. Fluid Mech., **237**, pp. 373–393.

[12] Madsen, J., Olhoff, N., and Condra, T., 2000, "Optimization of Straight, Two-Dimensional Diffusers by Wall Contouring and Guide Vane Insertion," Proceedings of the 3rd World Congress of Structural and Multidisciplinary Optimization, WCSMO-3, May 17–21, 1999, State University of New York at Buffalo, Buffalo.

[13] Liu, Z., Deng, Y., Lin, S., and Xuan, M., 2012, "Optimization of Micro Venturi Diode in Steady Flow at Low Reynolds Number," Eng. Optim., **44**(11), pp. 1389–1404.

[14] Borrvall, T., and Petersson, J., 2003, "Topology Optimization of Fluids in Stokes Flow," Int. J. Numer. Methods Fluids, **41**(1), pp. 77–107.

[15] Guest, J. K., and Prévost, J. H., 2006, "Topology Optimization of Creeping Fluid Flows Using a Darcy–Stokes Finite Element," Int. J. Numer. Methods Eng., **66**(3), pp. 461–484.

[16] Wiker, N., Klarbring, A., and Borrvall, T., 2007, "Topology Optimization of Regions of Darcy and Stokes Flow," Int. J. Numer. Methods Eng., **69**(7), pp. 1374–1404.

[17] Challis, V. J., and Guest, J. K., 2009, "Level Set Topology Optimization of Fluids in Stokes Flow," Int. J. Numer. Methods Eng., **79**(10), pp. 1284–1308.

[18] Evgrafov, A., 2006, "Topology Optimization of Slightly Compressible Fluids," ZAMM-J. Appl. Math. Mech./Z. Angew. Math. Mech., **86**(1), pp. 46–62.

[19] Gersborg-Hansen, A., Sigmund, O., and Haber, R. B., 2005, "Topology Optimization of Channel Flow Problems," Struct. Multidiscip. Optim., **30**(3), pp. 181–192.

[20] Olesen, L. H., Okkels, F., and Bruus, H., 2006, "A High-Level Programming-Language Implementation of Topology Optimization Applied to Steady-State Navier–Stokes Flow," Int. J. Numer. Methods Eng., **65**(7), pp. 975–1001.

[21] Duan, X.-B., Ma, Y.-C., and Zhang, R., 2008, "Shape-Topology Optimization for Navier–Stokes Problem Using Variational Level Set Method," J. Comput. Appl. Math., **222**(2), pp. 487–499.

[22] Zhou, S., and Li, Q., 2008, "A Variational Level Set Method for the Topology Optimization of Steady-State Navier–Stokes Flow," J. Comput. Phys., **227**(24), pp. 10178–10195.

[23] Kreissl, S., and Maute, K., 2012, “Levelset Based Fluid Topology Optimization Using the Extended Finite Element Method,” Struct. Multidiscip. Optim., **46**(3), pp. 311–326.
[24] Pingen, G., 2008, “Optimal Design for Fluidic Systems: Topology and Shape Optimization With the Lattice Boltzmann Method,” Ph.D. thesis, University of Colorado, Boulder.
[25] Pingen, G., Evgrafov, A., and Maute, K., 2008, “A Parallel Schur Complement Solver for the Solution of the Adjoint Steady-State Lattice Boltzmann Equations: Application to Design Optimisation,” Int. J. Comput. Fluid Dyn., **22**(7), pp. 457–464.
[26] Elman, H., Silvester, D., and Wathen, A., 2014, *Finite Elements and Fast Iterative Solvers: With Applications in Incompressible Fluid Dynamics*, Oxford University.
[27] Kreissl, S., and Maute, K., 2012, “Levelset Based Fluid Topology Optimization Using the Extended Finite Element Method,” Struct. Multidiscip. Optim., **46**(3), pp. 311–326.
[28] Sigmund, O., and Petersson, J., 1998, “Numerical Instabilities in Topology Optimization: A Survey on Procedures Dealing With Checkerboards, Mesh-Dependencies and Local Minima,” Struct. Optim., **16**(1), pp. 68–75.
[29] Guest, J. K., Prévost, J., and Belytschko, T., 2004, “Achieving Minimum Length Scale in Topology Optimization Using Nodal Design Variables and Projection Functions,” Int. J. Numer. Methods Eng., **61**(2), pp. 238–254.
[30] Sigmund, O., 2007, “Morphology-Based Black and White Filters for Topology Optimization,” Struct. Multidiscip. Optim., **33**(4–5), pp. 401–424.
[31] Guest, J. K., 2009, “Topology Optimization With Multiple Phase Projection,” Comput. Methods Appl. Mech. Eng., **199**(1), pp. 123–135.
[32] Sigmund, O., 1997, “On the Design of Compliant Mechanisms Using Topology Optimization,” J. Struct. Mech., **25**(4), pp. 493–524.
[33] Guest, J. K., Asadpoure, A., and Ha, S.-H., 2011, “Eliminating Beta-Continuation From Heaviside Projection and Density Filter Algorithms,” Struct. Multidiscip. Optim., **44**, pp. 443–453.
[34] Svanberg, K., 1987, “The Method of Moving Asymptotes—A New Method for Structural Optimization,” Int. J. Numer. Methods Eng., **24**, pp. 359–373.
[35] Sigmund, O., 2009, “Manufacturing Tolerant Topology Optimization,” Acta Mech. Sin., **25**(2), pp. 227–239.
[36] Guest, J. K., and Igusa, T., 2008, “Structural Optimization Under Uncertain Loads and Nodal Locations,” Comput. Methods Appl. Mech. Eng., **198**(1), pp. 116–124.
[37] Asadpoure, A., Tootkaboni, M., and Guest, J. K., 2011, “Robust Topology Optimization of Structures With Uncertainties in Stiffness–Application to Truss Structures,” Comput. Struct., **89**(11), pp. 1131–1141.
[38] Schevenels, M., Lazarov, B. S., and Sigmund, O., 2011, “Robust Topology Optimization Accounting for Spatially Varying Manufacturing Errors,” Comput. Methods Appl. Mech. Eng., **200**(49), pp. 3613–3627.
[39] Wang, F., Jensen, J. S., and Sigmund, O., 2011, “Robust Topology Optimization of Photonic Crystal Waveguides With Tailored Dispersion Properties,” J. Opt. Soc. Am. B, **28**(3), pp. 387–397.